Partial-wave decomposition of the Keldysh ionization amplitude

S. Walker,* B. Ghomashi, and A. Becker
JILA and Department of Physics, University of Colorado, Boulder, Colorado 80309-0440, USA

(Received 26 July 2023; accepted 12 October 2023; published 1 November 2023)

We present an alternative way of calculating the Keldysh amplitude, i.e., the length-gauge form of the ionization amplitude in the strong-field approximation. The amplitude is evaluated exactly by expanding it in Fourier components and partial waves. Comparisons of the semianalytic model predictions with results of *ab initio* numerical simulations of the time-dependent Schrödinger equation for the interaction of electrons in short-range potentials with intense laser light yield excellent agreement, for wavelengths from the single photon to the multiphoton to the tunneling regime. Specifically, for ionization from initial states with higher angular momentum quantum number, e.g., *p* states, a significant improvement over predictions based on the popular saddle-point approximation is found. Furthermore, the current model rate allows for interpretation of the strong-field ionization process in terms of multiphoton absorption pathways and angular momentum selection rules.

DOI: 10.1103/PhysRevA.108.053102

I. INTRODUCTION

The interaction of matter with strong electromagnetic radiation in the form of short laser pulses has been a fundamental topic in quantum dynamics of atoms, molecules, and solids for the past few decades. Applications of such laser pulses are found in many different areas of atomic, molecular, and optical physics, solid-state physics, nanomaterials, plasma physics, chemistry, biology, etc. Frequencies of currently available short-pulsed laser systems range from the far infrared through the optical and the vacuum ultraviolet up to the soft x-ray region. The focused laser intensities reach levels far beyond the strength of the Coulomb fields that bind electrons and nuclei together, while the pulse lengths have decreased to femtoseconds (10^{-15} s) and more recently even below into the attosecond (10^{-18} s) regime.

An analytical solution of the Schrödinger equation for the interaction of an atom (or molecule, solid) with short-pulsed electromagnetic radiation has not been found so far. However, for rather simple systems numerical integration techniques and Floquet methods exist [1,2]. In view of the computational costs to perform such numerical *ab initio* calculations, approximation methods are useful to analyze strong-field processes. Perhaps the most popular one is the lowest order of a systematic *S*-matrix series, known as the strong-field approximation (or, Keldysh-Faisal-Reiss theory [3–5]). In its basic form the first-order term for ionization of an electron from an atom exhibits the transition from the unperturbed initial state in the atom via the interaction with the field (in either the length- or the velocity-gauge form) into the final Volkov states, i.e., the states of a free electron in the laser field. The ionization amplitude is then often further evaluated in length gauge via the classical action using the so-called stationary phase or saddle-point approximation [3,6]. This leads to an analytical form of the amplitude that can be easily computed, is typically applied in the low-frequency regime, and often reveals an intuitive picture of the process via classical trajectories.

Recent developments in strong-field physics, e.g., the application of laser sources, such as free electron lasers [7] and high harmonic sources [8], have extended the wavelength regime, accessible for strong laser light, from the ultraviolet to the (soft) x-ray regime. Moreover, it has become possible to control the polarization state of such pulses, enabling studies not only with linearly polarized, but elliptically and circularly polarized light [9,10]. This makes it necessary to consider alternative evaluations of the ionization amplitude, which may extend the application regime of the standard approximation methods.

In this work we present an alternative method to evaluate the ionization amplitude in the strong-field approximation. Several choices made in the derivation are motivated as follows. First, we choose to work with the length-gauge amplitude [3,11,12]. This is motivated by the recent interest in laser-mediated applications involving chiral processes [13–22] where the helicity of the ground state is coupled to the helicity of the applied field during ionization. Velocity gauge decouples these motions and does not consider the dependence of the ionization rate on the sign of the magnetic quantum number of the initial state [5]. Next, we apply the initial-state Lippmann-Schwinger-type expansion of the Keldysh amplitude [3] instead of the final-state expansion of Perelomov, Popov, and Terent'ev (PPT) [12] to allow for modification of the final state [23]. We may note that the Keldysh and PPT models are identical in the limit of zero-range potentials but deviate for finite-range applications (see discussion in Appendix A). Finally, our approach involves expanding the Keldysh ionization amplitude in Fourier components (in time) and partial waves (in space), in this way we circumvent

*Present address: Department of Physics, The Ohio State University, Columbus, Ohio 43210, USA; walker.2190@osu.edu

the stationary phase approximation in length-gauge calculations. As we will show below, this improves the agreement with results of *ab initio* numerical simulations in the case of initial states with angular momentum quantum number $l_i \neq 0$ significantly. Our exact evaluation of the ionization amplitude is motivated by the partial-wave expansion [24–31] used in nuclear physics and scattering theory as well as the strong-field expansion given in Refs. [5,32].

As an application to test the predictions of our approach, we use the ionization of electrons bound in s and p states of short-range potentials by circularly, elliptically, and linearly polarized light at wavelengths from 10–800 nm. The applications include the reversal of ionization ratio of co- to counterrotating electrons (with respect to the rotation direction of the applied field) in the intermediate few-photon ionization regime, which has been a topic of recent research in experiment and theory [13–20]. As we will show below, our semianalytical formula provides excellent results for the ionization of electrons bound to short-range potentials in the presence of strong circularly, elliptically, and linearly polarized fields at nonperturbative intensities over a broad wavelength regime, from single-photon to tunneling ionization. Furthermore, the results let us describe the strong-field ionization process in terms of multiphoton absorption pathways and angular momentum selection rules.

The rest of the paper is organized as follows. In Sec. II we first briefly review the Keldysh amplitude and the popular saddle-point approximation. We then continue by presenting the formula resulting from an evaluation based on expansions in Fourier components and partial waves. This is first done for circular polarization and then for the general case of elliptical polarization. In the main text we present the main formula while the detailed derivation is presented and discussed in the Appendixes. In the second part (Sec. III) we present applications in the form of comparisons of the model predictions with results of *ab initio* numerical simulations of the time-dependent Schrödinger equation. Furthermore, general trends for the photoelectron energy and angular distributions will be presented and further approximations will be discussed. The paper ends with a brief summary.

II. IONIZATION AMPLITUDE

We seek to provide an alternative semianalytic approximative solution of the time-dependent Schrödinger equation (TDSE)

$$i\hbar\frac{\partial}{\partial t}\Psi_\epsilon(\mathbf{r},t) = [H_a + |e|\mathbf{E}_\epsilon(t)\cdot\mathbf{r}]\Psi_\epsilon(\mathbf{r},t) \tag{1}$$

for the interaction of an atomic system in a short-range potential with an elliptically polarized laser pulse with electric field and vector potential given by

$$\mathbf{E}_\epsilon(t) = E\,[\cos(\omega t)\hat{\mathbf{x}} + \epsilon\sin(\omega t)\hat{\mathbf{y}}], \tag{2}$$

and

$$\mathbf{A}_\epsilon(t) = -A\,[\sin(\omega t)\hat{\mathbf{x}} - \epsilon\cos(\omega t)\hat{\mathbf{y}}], \tag{3}$$

where $A = \frac{cE}{\omega}$. We write the vector potential as a linear combination of both right-handed (+) and left-handed (–) circularly polarized fields

$$\mathbf{A}_\epsilon(t) = \left(\frac{1+\epsilon}{2}\right)\mathbf{A}_+(t) + \left(\frac{1-\epsilon}{2}\right)\mathbf{A}_-(t). \tag{4}$$

In this way we can use the same steps to determine the ionization amplitude first for circularly polarized fields and then for elliptically polarized fields.

Our approach is based on the Keldysh ionization amplitude. In Sec. II A we will therefore briefly review its derivation and discuss our selection of initial atomic and final Volkov states. Then, in Sec. II B, we first briefly discuss the traditional semiclassical low-frequency approach and then develop our alternative approach of evaluating the amplitude, based on expanding the amplitude in discrete energy levels and partial waves, first for circular polarization and then for the general case of elliptical polarization. We take the long pulse limit and determine the ionization rate and angular emission rate for each photon process.

A. Keldysh amplitude

The exact solution to the TDSE can be expressed as the Lippmann-Schwinger-type integral equation

$$\Psi(x) = \phi_i(x) + \int d^4x_1\; G(x;x_1)V_L(x_1)\phi_i(x_1) \tag{5}$$

for an arbitrary field where we use the notation

$$\int d^4x_1 \equiv \int_{t_0}^{t} dt_1 \int d\mathbf{r}_1 \tag{6}$$

for integration over intermediate coordinates. Here t_0 is the moment when the field is turned on and t is the instant in time when the field is turned off.

The initial atomic state is either chosen to be the exact numerical eigenstates for a single active electron (SAE) potential

$$\phi_i(x) \equiv e^{(i/\hbar)I_p t}\phi_i(\mathbf{r}) = e^{(i/\hbar)I_p t}R_i(r)Y_{l_i}^{m_i}(\mathbf{r}) \tag{7}$$

with R_i given by

$$H_a(\mathbf{r})\phi_i(\mathbf{r}) = \left[\frac{\mathbf{p}_{\rm op}^2}{2m} + V_a(\mathbf{r})\right]\phi_i(\mathbf{r}) = -I_p\phi_i(\mathbf{r}) \tag{8}$$

with atomic potential $V_a(\mathbf{r})$ and momentum operator $\mathbf{p}_{\rm op} = -i\hbar\nabla_{\mathbf{r}}$ or the approximate asymptotic states from Ref. [12], where

$$R_i(r) \approx C_{\kappa l_i}\kappa^{3/2}(\kappa r)^{\nu-1}e^{-\kappa r}, \tag{9}$$

which is accurate for calculations at long wavelengths where ionization is dominated by the tail ($\kappa r \gg 1$) of the ground state. I_p is the ionization potential, $\hbar\kappa \equiv \sqrt{2mI_p}$ is the bound-state momentum, and we obtain $C_{\kappa l_i}$ by fitting the asymptotic

state to the long-range part ($\kappa r \gg 1$) of the exact state. We will focus on accurate solutions for the case of short-range potentials where the solution to the atomic Schrödinger equation for $\kappa r \gg 1$ gives the zero-range approximation $\nu = 0$ in Eq. (9). Long-range potentials will briefly be discussed where the power law becomes $\nu \equiv (\kappa_C/\kappa)$ with the Coulomb momentum $\hbar\kappa_C = mZ|e|^2/\hbar$ and residual ionic charge $Z|e|$.

The ionization amplitude is derived by expanding the Green's function in Eq. (5) in finite-range or zero-range Volkov states and projecting on it:

$$\mathcal{M}(\mathbf{k},t) = \int d\mathbf{r}\, \overline{\Phi_{\mathbf{k}}^{(-)}(x)}\Psi(x), \tag{10}$$

where horizontal lines above symbols are used to represent the complex conjugate. The zeroth-order contribution

$$\mathcal{M}^{(0)}(\mathbf{k},t) = \int d\mathbf{r}\, \overline{\Phi_{\mathbf{k}}^{(-)}(x)}\phi_i(x) \tag{11}$$

is identically zero for finite-range Volkov states and dies off for zero-range Volkov states in the long pulse limit [12]. The lowest-order contribution therefore arises from

$$\mathcal{M}^{(1)}(\mathbf{k},t) = -\left(\frac{i}{\hbar}\right)\int d^4x_1 \overline{\Phi_{\mathbf{k}}^{(-)}(x_1)}[|e|\mathbf{E}(t_1)\cdot\mathbf{r}_1]\phi_i(x_1), \tag{12}$$

which is the well-known Keldysh amplitude [3].

B. Evaluation of Keldysh amplitude

1. Standard low-frequency semiclassical approach

Usually, the ionization rate is then evaluated by writing it as [3,12,15]

$$\begin{aligned} w &= \lim_{t\to\infty}\int d\mathbf{k}\,\frac{\partial}{\partial t}|\mathcal{M}^{(1)}(\mathbf{k},t)|^2 \\ &= \lim_{t\to\infty}\int d\mathbf{k}\,\frac{\partial}{\partial t}|\mathcal{M}^{(1,\mathrm{PPT})}(\mathbf{k},t)|^2 \end{aligned} \tag{13}$$

using the amplitude given by Perelomov, Popov, and Terent'ev (PPT)

$$\mathcal{M}^{(1,\mathrm{PPT})}(\mathbf{k},t) = -\left(\frac{i}{\hbar}\right)\int d^4x_1 \overline{\Phi_{\mathbf{k}}(x_1)}V_a(\mathbf{r})\phi_i(x_1). \tag{14}$$

We note that the PPT and Keldysh rates are equivalent when zero-range Volkov states are used, as shown in Appendix A. After taking the limit the rate simplifies to:

$$w = \frac{2\pi}{\hbar}\int d\mathbf{k}\sum_{n=-\infty}^{\infty}|L_n(\mathbf{k})|^2\delta(E_k + \tilde{I}_p - n\hbar\omega), \tag{15}$$

where $E_k \equiv \hbar^2k^2/2m$ defines the kinetic energy of liberated electrons and

$$L_n(\mathbf{k})|_{k=k_n} \equiv \frac{\omega}{2\pi}\int_{-\pi/\omega}^{\pi/\omega} dt\, S'(\mathbf{k},t)\, e^{(i/\hbar)S(\mathbf{k},t)}\tilde{\phi}_i(\mathbf{k}(t))\Big|_{k=k_n} \tag{16}$$

for zero-range final Volkov states $\Phi_{\mathbf{k}}$ and zero-range initial bound states ϕ_i defined in Eq. (9) with momentum representation

$$\tilde{\phi}_i(\mathbf{k}(t)) = \int d\mathbf{r}\,\frac{e^{-i\mathbf{k}(t)\cdot\mathbf{r}}}{(2\pi)^{3/2}}\phi_i(\mathbf{r}). \tag{17}$$

Here

$$S(\mathbf{k},t) = \int_{t_0}^{t} d\tau\left[\frac{\mathbf{p}(\tau)^2}{2m} + I_p\right] \tag{18}$$

defines the classical action with kinetic momentum

$$\mathbf{p}(t) = \hbar\mathbf{k}(t) = \hbar\mathbf{k} + \frac{|e|}{c}\mathbf{A}(t) \tag{19}$$

and the ponderomotive or cycle-averaged quiver energy

$$U_p = \frac{|e|^2}{2mc^2}\langle\mathbf{A}(t)^2\rangle_T \tag{20}$$

determines the effective ionization potential $\tilde{I}_p \equiv I_p + U_p$ where primes denote derivatives with respect to t.

For laser parameters where the photon energy satisfies $\hbar\omega \ll I_p$ and $\hbar\omega \ll U_p$ one can then perform the stationary phase approximation [3,6]. This semiclassical approach involves determining saddle points t_s, which satisfy the conservation law

$$S'(\mathbf{k},t_s) = \frac{\mathbf{p}(t_s)^2}{2m} + I_p = 0 \tag{21}$$

and approximates the time integral in Eq. (16) as a finite sum over all saddle points

$$\begin{aligned} L_n(\mathbf{k})|_{k=k_n} \equiv \frac{\omega}{2\pi}\sum_{t_s}\sqrt{\frac{2\pi i\hbar}{S''(\mathbf{k},t_s)}} \\ \times\, S'(\mathbf{k},t_s)\, e^{(i/\hbar)S(\mathbf{k},t_s)}\tilde{\phi}_i(\mathbf{k}(t_s))|_{k=k_n}. \end{aligned} \tag{22}$$

Contributions $L_n(\mathbf{k})|_{k=k_n}$ are nonzero since $\tilde{\phi}_i(\mathbf{k}(t_s))$ contains poles that coincide with the zeros of $S'(\mathbf{k},t_s)$.

2. Exact time integration and expansion in partial waves: Circular polarization

In order to extend the application of the Keldysh amplitude into the regime $\hbar\omega \gtrsim I_p$ or $\hbar\omega \gtrsim U_p$ a different approach is required. To this end, we select $t_0 = 0$ and write the amplitude as

$$\mathcal{M}^{(1)}(\mathbf{k},t) = \int_0^t dt_1 e^{(i/\hbar)S(\mathbf{k},t_1)}\left(-\frac{\partial}{\partial t_1}\right)\tilde{\phi}_i(\mathbf{k},\mathbf{A}(t_1)) \tag{23}$$

described by the bound-state momentum component

$$\tilde{\phi}_i(\mathbf{k},\mathbf{A}(t_1)) = \int d\mathbf{r}_1\overline{\phi_{\mathbf{k}}^{(-)}(\mathbf{r}_1)}e^{-\frac{i|e|}{\hbar c}\mathbf{A}(t_1)\cdot\mathbf{r}_1}\phi_i(\mathbf{r}_1) \tag{24}$$

and phase factors $e^{(i/\hbar)S(\mathbf{k},t_1)}$ at ionization time t_1. We then expand the terms in Eq. (23) in partial waves to determine the ionization amplitude in the case of circular

polarization as (see Appendix B):

$$\mathcal{M}_{\pm}^{(1)}(\mathbf{k},t) = (i/\hbar)e^{-i\mathbf{k}\cdot\boldsymbol{\xi}_{\pm}(0)} \sum_{l_A=0}^{\infty}\sum_{n_A=-l_A}^{l_A} (n_A\hbar\omega)A_{l_A}^{m_A} \sum_{l_k=\max(|l_i-l_A|,|m_i+m_A|)}^{l_i+l_A} K_{l_k}(k)\, I_{l_i}^{l_k,l_A}(k) \begin{bmatrix} l_k & l_A & l_i \\ -(m_i+m_A) & m_A & m_i \end{bmatrix} Y_{l_k}^{m_i+m_A}(\hat{\mathbf{k}})$$
$$\times \sum_{l_S=0}^{\infty}\sum_{n_S=-l_S}^{l_S} X_{l_S}^{m_S}(k) Y_{l_S}^{m_S}(\hat{\mathbf{k}})\delta_t([N(k)-(n_A+n_S)]\omega/2), \tag{25}$$

where $\boldsymbol{\xi}_{\pm}(0) = \xi\hat{\mathbf{x}}$ in the present case of circular polarization with $\xi = \frac{|e|A}{\omega mc}$ as the quiver radius and $\hbar k_A \equiv (|e|/c)A$ is the vector potential momentum. $N(k) \equiv \frac{1}{\hbar\omega}(E_k + \tilde{I}_p)$ corresponds to the number of absorbed photons for an ejected electron with kinetic energy $E_k = \frac{\hbar^2k^2}{2m}$, while l_i and m_i are the orbital and magnetic angular momentum quantum numbers of the initial state. Furthermore,

$$A_{l_A}^{m_A} \equiv 4\pi(-i)^{l_A}\,\overline{Y_{l_A}^{m_A}(\hat{\mathbf{A}}_{\pm}(0))}, \tag{26}$$

where $Y_{l_A}^{m_A}(\hat{\mathbf{A}}_{\pm}(0))$ are the spherical harmonics with $m_A \equiv \pm n_A$,

$$K_{l_k}(k) \equiv (-i)^{l_k} e^{i\eta_{l_k}(k)} \tag{27}$$

with $\eta_{l_k}(k)$ as the phase shift of the continuum state,

$$X_{l_S}^{m_S}(k) \equiv 4\pi i^{l_S} j_{l_S}(k\xi)\overline{Y_{l_S}^{m_S}(\hat{\boldsymbol{\xi}}_{\pm}(0))} \tag{28}$$

with spherical Bessel function $j_{l_S}(k\xi)$ in addition to $m_S \equiv \pm n_S$, with line shape

$$\delta_t(x) \equiv e^{ixt}\,\mathrm{sinc}(xt)t \tag{29}$$

and radial function

$$I_{l_i}^{l_k,l_A}(k) \equiv \frac{1}{k}\int_0^{\infty} dr\, r^2\, R_{k,l_k}(r) j_{l_A}(k_A r) R_i(r) \tag{30}$$

with $R_{k,l_k}(r)$ and $R_i(r)$ as the radial parts of the continuum state and the initial bound state, respectively.

The angular momentum components are determined by

$$\begin{bmatrix} l_k & l_A & l_i \\ -m_k & m_A & m_i \end{bmatrix} \equiv \int d\Omega_{r_1} \overline{Y_{l_k}^{m_k}(\hat{\mathbf{r}}_1)} Y_{l_A}^{m_A}(\hat{\mathbf{r}}_1) Y_{l_i}^{m_i}(\hat{\mathbf{r}}_1) \tag{31}$$

and the yield is given by

$$P_{\pm}^{(\mathrm{ion})}(t) = \int d\mathbf{k}\, |\mathcal{M}_{\pm}(\mathbf{k},t)|^2. \tag{32}$$

3. Long pulse limit

The time-averaged rate for a long pulse can be determined in the usual way by taking the limit in time

$$W_{\pm}(\mathbf{k}) = \lim_{t\to\infty} t^{-1}|\mathcal{M}_{\pm}^{(1)}(\mathbf{k},t)|^2 \equiv \sum_{n=n_{\mathrm{th}}}^{\infty} |\mathcal{M}_{n\pm}^{(1)}(\hat{\mathbf{k}})|^2 \delta(k-k_n) \tag{33}$$

and using the sinc representation of the Dirac delta function, which results in the quantized final-state momenta

$$\hbar k_n \equiv \sqrt{2m(n\hbar\omega - \tilde{I}_p)} \equiv m v_n \tag{34}$$

and the total rate

$$w_{\pm} = \int d\mathbf{k}\, W_{\pm}(\mathbf{k}) = \sum_{n=n_{\mathrm{th}}}^{\infty}\int d\Omega_k \frac{dw_{n\pm}}{d\Omega_k}$$
$$= \sum_{n=n_{\mathrm{th}}}^{\infty}\sum_{l=|m_i\pm n|}^{\infty} w_{ln\pm} = \sum_{n=n_{\mathrm{th}}}^{\infty} w_{n\pm} \tag{35}$$

after the absorption of n photons with threshold value $n_{\mathrm{th}} = \lceil \tilde{I}_p/\hbar\omega \rceil$. Above we introduced the partial rates

$$w_{ln\pm} = k_n^2 \left|C_l^{m_i\pm n}(k_n)\right|^2 \quad \text{and} \quad w_{n\pm} = \sum_{l=|m_i\pm n|}^{\infty} w_{ln\pm} \tag{36}$$

as well as the angular rates

$$\frac{dw_{n\pm}}{d\Omega_k} = k_n^2 |\mathcal{M}_{\pm}(\mathbf{k}_n)|^2 \quad \text{and} \quad \frac{dw_{\pm}}{d\Omega_k} = \sum_{n=n_{\mathrm{th}}}^{\infty}\frac{dw_{n\pm}}{d\Omega_k} \tag{37}$$

with

$$\mathcal{M}_{\pm}^{(1)}(\mathbf{k}_n) = e^{-i\mathbf{k}_n\cdot\boldsymbol{\xi}_{\pm}(0)} \sum_{l=|m_i\pm n|}^{\infty} C_l^{m_i\pm n}(k_n) Y_l^{m_i\pm n}(\hat{\mathbf{k}}_n) \tag{38}$$

where the coefficients are given by

$$C_l^{m_i\pm n}(k_n) \equiv (i/\hbar)\sqrt{\frac{2\pi}{v_n}} \sum_{l_A=0}^{\infty}\sum_{n_A=-l_A}^{l_A} (n_A\hbar\omega)A_{l_A}^{m_A} \sum_{l_k=\max(|l_i-l_A|,|m_i+m_A|)}^{l_i+l_A} K_{l_k}(k_n)\, I_{l_i}^{l_k,l_A}(k_n) \begin{bmatrix} l_k & l_A & l_i \\ -(m_i+m_A) & m_A & m_i \end{bmatrix}$$
$$\times \sum_{l_S=|m_S|}^{\infty} X_{l_S}^{m_S}(k_n) \begin{bmatrix} l & l_S & l_k \\ -(m_i+m_A+m_S) & m_S & (m_i+m_A) \end{bmatrix} \tag{39}$$

with $n_S = n - n_A$, enforced by the $t \to \infty$ limit. For a long, but finite pulse the total ionization yield can be approximated as

$$N_{\mathrm{ion}} = 1 - e^{-wT}, \tag{40}$$

where T is the pulse duration.

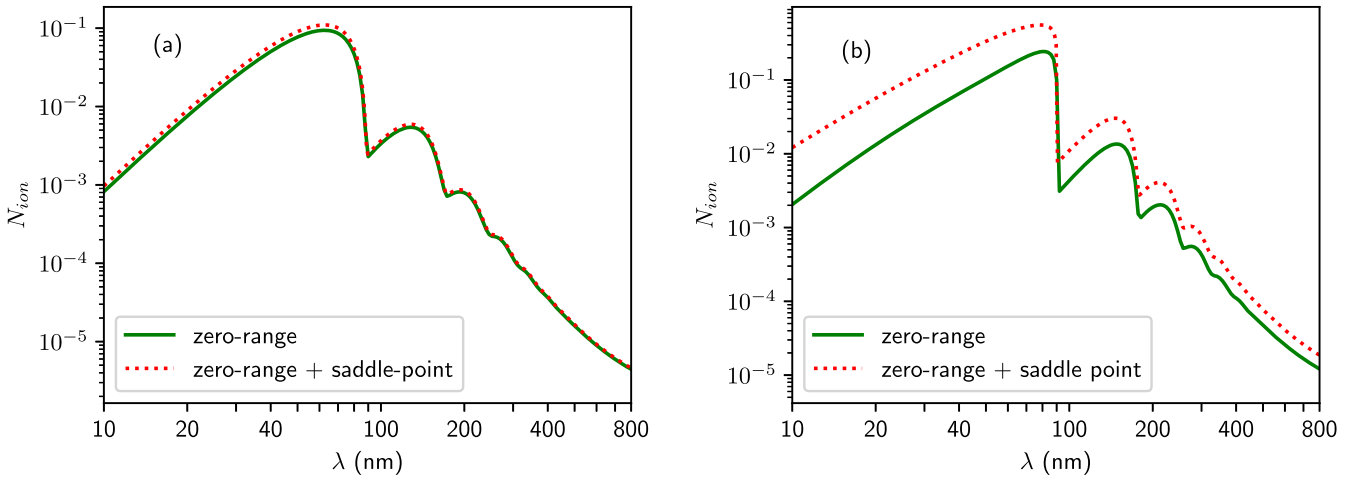

FIG. 1. Total ionization yield for the length-gauge amplitude corresponding to a 16 cycle laser pulse with an intensity of $10^{14}\,\mathrm{W/cm^2}$ for zero-range Volkov states and zero-range asymptotic bound states. Results are compared between the saddle-point approximation (red dashed curve) and the exact time integration (green solid curve) for s states (a) and total yield from the sum of all p states (b). All zero-range states have an ionization potential of $I_p \approx 13.6$ eV.

4. Comparison with the saddle-point approximation

Before we proceed, we assess the difference between the results of the two evaluations of the Keldysh amplitude. To this end, we have performed calculations for the laser-induced ionization of an electron bound in a zero-range potential using both the standard saddle-point approximation and our approach. For the comparison we have chosen zero-range Volkov final states and considered the zero-range asymptotic initial states of different angular momentum from Eq. (9) and a binding energy $I_p \approx 13.6$ eV.

In Fig. 1 we compare the saddle-point PPT result (equivalent to Eqs. (76)–(78) of Ref. [15]) to the same amplitude without the approximation for the ionization of an electron in an initial s state (left panel) and an initial p state (right panel) due to the interaction with 16 cycle circularly polarized laser pulses ($T = 16 \times \frac{2\pi}{\omega}$), having an intensity of $10^{14}\,\mathrm{W/cm^2}$ and wavelengths between 10 nm and 800 nm. Equivalence between our evaluation of the Keldysh amplitude and a similar exact evaluation of the PPT amplitude is demonstrated in Appendix A. The comparison shown in Fig. 1 therefore outlines the errors introduced by approximating the integral over ionization times with the saddle-point approximation.

From the comparison it is obvious that in the case of an s state for nearly all wavelengths longer than the single-photon ionization threshold (∼92 nm), both the exact (green curve) and approximate amplitude (red dashed curve) predict essentially the same results.

In contrast, the same comparison for the sum of all initial p states with

$$N_{\mathrm{ion}}^{(j)} = 1 - e^{-w^{(j)}T} \tag{41}$$

as before and

$$N_{\mathrm{ion}} = N_{\mathrm{ion}}^{(2p_1)} + N_{\mathrm{ion}}^{(2p_0)} + N_{\mathrm{ion}}^{(2p_{-1})} \tag{42}$$

shows that the exact (green curve) and approximate amplitude (red dashed curve) disagree over almost the entire wavelength regime considered.

Comparison of the exact evaluation of the zero-range model with finite-range numerical solutions of the TDSE will be discussed in Sec. III A, where we will show the accurateness of the present calculations. In particular, we note that the s-state results of Fig. 1(a) are included in Fig. 2(a) and the p-state results of Fig. 1(b) are included in Fig. 3(c) and show acceptable levels of agreement with the TDSE results.

5. Exact time integration and expansion in partial waves: Elliptical polarization

By writing the field in the general case of elliptical polarization as a linear combination of two circularly polarized fields, as discussed at the outset of this section, similar steps can be taken to determine the ionization rate for the interaction with an elliptically polarized field (see Appendix C):

$$\begin{aligned}\mathcal{M}_{\epsilon}^{(1)}(\mathbf{k},t) = (i/\hbar)e^{-i\mathbf{k}\cdot\boldsymbol{\xi}_{\epsilon}(0)} \sum_{\mathbf{l}_A,\mathbf{n}_A} (n_A\hbar\omega) A_{\mathbf{l}_A}^{\mathbf{m}_A} \sum_{l_k} K_{l_k}(k) I_{l_i}^{l_k,\mathbf{l}_A}(k,k_A,\epsilon) \begin{bmatrix} l_k & \mathbf{l}_A & l_i \\ -(m_i+m_A) & \mathbf{m}_A & m_i \end{bmatrix} \\ \times \sum_{\mathbf{l}_S,\mathbf{n}_S} X_{\mathbf{l}_S}^{\mathbf{m}_S}(k,\xi,\epsilon) \sum_{l} \begin{bmatrix} l & \mathbf{l}_S & l_k \\ -(m_i+m_A+m_S) & \mathbf{m}_S & (m_i+m_A) \end{bmatrix} Y_l^{m_i+m_A+m_S}(\hat{\mathbf{k}}) \\ \times \sum_{a} B_a(A,\omega,\epsilon)\delta_t([N(k)-(n_A+n_S+2a)]\omega/2),\end{aligned} \tag{43}$$

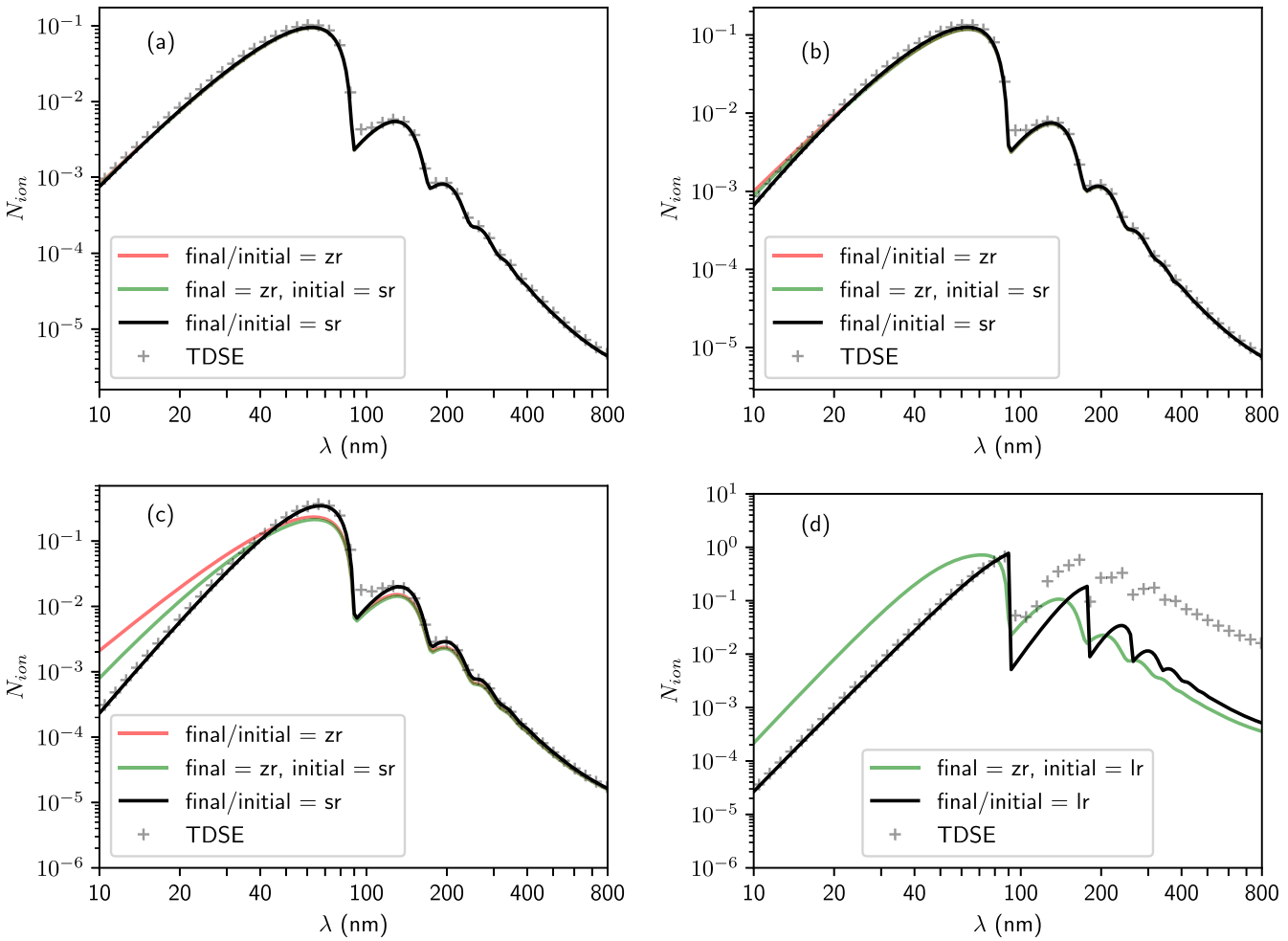

FIG. 2. Comparison of predictions for the s-state model with the TDSE results for exponential parameters $a = a_0/5$, $a_0/3$, a_0, and ∞ (a)–(d). The red line corresponds to calculations using zero-range (zr) initial bound and final Volkov states. The green curve replaces the zero-range initial states with the short-range (sr) states of the atomic Hamiltonian. The black curve corresponds to calculations with the same short-range initial states, but now the zero-range Volkov states have been replaced with short-range Volkov states. $a = \infty$ is included for an initial ground state of hydrogen with final zero-range Volkov states (green) and long-range (lr) Coulomb-Volkov scattering states (black). Laser parameters and bound-state energies are identical to Fig. 1.

where

$$X_{\mathbf{l}_S}^{\mathbf{m}_S}(k,\xi,\epsilon) \equiv 16\pi^2 i^{l_S} j_{l_{S_-}}\left[\left(\frac{1-\epsilon}{2}\right)k\xi\right] j_{l_{S_+}}\left[\left(\frac{1+\epsilon}{2}\right)k\xi\right]\overline{Y_{l_{S_-}}^{-n_{S_-}}(\hat{\boldsymbol{\xi}}_-(0))Y_{l_{S_+}}^{n_{S_+}}(\hat{\boldsymbol{\xi}}_+(0))}, \tag{44}$$

$$A_{\mathbf{l}_A}^{\mathbf{m}_A} = 16\pi^2(-i)^{l_A}\overline{Y_{l_{A_-}}^{-n_{A_-}}(\hat{\mathbf{A}}_-(0))}\,\overline{Y_{l_{A_+}}^{n_{A_+}}(\hat{\mathbf{A}}_+(0))}, \tag{45}$$

$$K_{l_k}(k) = (-i)^{l_k} e^{i\eta_{l_k}(k)} \tag{46}$$

and

$$B_a(A,\omega,\epsilon) = J_a\left(\frac{|e|^2A^2(1-\epsilon^2)}{8\hbar\omega mc^2}\right) \tag{47}$$

with $\mathbf{n}_A \equiv (n_{A_-}, n_{A_+})$, $n_A \equiv n_{A_+} + n_{A_-}$, $\mathbf{m}_A \equiv (-n_{A_-}, n_{A_+})$, $m_A \equiv n_{A_+} - n_{A_-}$, $\mathbf{l}_A \equiv (l_{A_-}, l_{A_+})$ and $l_A \equiv l_{A_+} + l_{A_-}$ with similar for $A \mapsto S$. Additionally the shorthand notations

$$\sum_{\mathbf{l}_A,\mathbf{n}_A} \equiv \sum_{l_{A_+}=0}^{\infty}\sum_{n_{A_+}=-l_{A_+}}^{l_{A_+}}\sum_{l_{A_-}=0}^{\infty}\sum_{n_{A_-}=-l_{A_-}}^{l_{A_-}} \tag{48}$$

and

$$\sum_{\mathbf{l}_S,\mathbf{n}_S} \equiv \sum_{l_{S_+}=0}^{\infty} \sum_{n_{S_+}=-l_{S_+}}^{l_{S_+}} \sum_{l_{S_-}=0}^{\infty} \sum_{n_{S_-}=-l_{S_-}}^{l_{S_-}} \tag{49}$$

have been used to simplify the sums. The angular contribution becomes

$$\begin{bmatrix} l_k & \mathbf{l}_A & l_i \\ -m_k & \mathbf{m}_A & m_i \end{bmatrix} \equiv \int d\Omega_r \overline{Y_{l_k}^{m_k}(\hat{\mathbf{r}})} Y_{l_{A_-}}^{-n_{A_-}}(\hat{\mathbf{r}}) Y_{l_{A_+}}^{n_{A_+}}(\hat{\mathbf{r}}) Y_{l_i}^{m_i}(\hat{\mathbf{r}}) \tag{50}$$

and

$$I_{l_i}^{l_k,\mathbf{l}_A}(k,k_A,\epsilon) \equiv \frac{1}{k}\int_0^\infty dr_1\, r_1^2\, R_{k,l_k}(r_1)\, j_{l_{A_-}}\left[\left(\frac{1-\epsilon}{2}\right)k_A r_1\right] j_{l_{A_+}}\left[\left(\frac{1+\epsilon}{2}\right)k_A r_1\right] R_{n_i,l_i}(r_1) \tag{51}$$

determines the radial behavior.

Taking the long-pulse limit as in Sec. II B 3 we obtain the amplitude for elliptical polarization:

$$\begin{aligned}\mathcal{M}_{n\epsilon}^{(1)}(\mathbf{k}_n) &= (i/\hbar)\sqrt{\frac{2\pi}{v_n}} e^{-i\mathbf{k}_n\cdot\boldsymbol{\xi}_\epsilon(0)} \sum_{\mathbf{l}_A,\mathbf{n}_A} (n_A\hbar\omega) A_{\mathbf{l}_A}^{\mathbf{m}_A} \sum_{l_k} K_{l_k}(k_n) I_{l_i}^{l_k,\mathbf{l}_A}(k_n,k_A,\epsilon) \begin{bmatrix} l_k & \mathbf{l}_A & l_i \\ -(m_i+m_A) & \mathbf{m}_A & m_i \end{bmatrix} \\ &\times \sum_a B_a(A,\omega,\epsilon) {\sum_{\mathbf{l}_S,\mathbf{n}_S}}' X_{\mathbf{l}_S}^{\mathbf{m}_S}(k_n,\xi,\epsilon) \sum_l Y_l^{m_i+m_A+m_S}(\hat{\mathbf{k}}_n) \begin{bmatrix} l & \mathbf{l}_S & l_k \\ -(m_i+m_A+m_S) & \mathbf{m}_S & (m_i+m_A) \end{bmatrix} \\ &= e^{-i\mathbf{k}_n\cdot\boldsymbol{\xi}_\epsilon(0)} \sum_{l,m} C_l^m(k_n) Y_l^m(\hat{\mathbf{k}}_n)\end{aligned} \tag{52}$$

with

$${\sum_{\mathbf{l}_S,\mathbf{n}_S}}' \equiv \sum_{l_{S_+}=0}^{\infty} \sum_{n_{S_+}=-l_{S_+}}^{l_{S_+}} \sum_{l_{S_-}=|n_{S_-}|}^{\infty}, \tag{53}$$

$$W_\epsilon(\mathbf{k}) = \sum_{n=n_{\rm th}}^{\infty} |\mathcal{M}_{n\epsilon}^{(1)}(\hat{\mathbf{k}})|^2 \delta(k-k_n), \tag{54}$$

$$\begin{aligned} w_\epsilon &= \int d\mathbf{k}\, W_\epsilon(\mathbf{k}) = \sum_{n=n_{\rm th}}^{\infty} \int d\Omega_k \frac{dw_{n\epsilon}}{d\Omega_k} \\ &= \sum_{n=n_{\rm th}}^{\infty} \sum_{l,m} w_{ln\epsilon}^m = \sum_{n=n_{\rm th}}^{\infty} w_{n\epsilon}, \end{aligned} \tag{55}$$

$$\frac{dw_{n\epsilon}}{d\Omega_k} = k_n^2 \left|\mathcal{M}_{n\epsilon}^{(1)}(\hat{\mathbf{k}}_n)\right|^2, \quad \text{and} \quad w_{ln\epsilon}^m = k_n^2 \left|C_l^m(k_n)\right|^2, \tag{56}$$

where

$$n_{S_-} = n - n_A - n_{S_+} - 2a \tag{57}$$

is enforced by the $t \to \infty$ limit. We may finally note that the partial-wave expansions used throughout are applicable to other gauges as well.

III. APPLICATIONS

In this section we first show comparisons of the model predictions for the ionization yields with results of simulations of the time-dependent Schrödinger equation. Furthermore, we give examples of predictions for the energy and angular distributions, which show the general features expected for light-induced processes.

A. Ionization yields

To test the model predictions we compare ionization yields of spinless hydrogen-like and neon-like anions using Eq. (35) and Eq. (55) with results of the time-dependent Schrödinger equation. In our test calculations we have used short-range Yukawa potentials of the form

$$V_a(\mathbf{r}) = -\frac{Z_a|e|^2}{r} e^{-r/a}, \tag{58}$$

where the exponential factor a determines the range of the potential and the prefactor Z_a is chosen such that the binding energy of $I_p \approx 13.6$ eV remains the same for all ranges considered. Comparisons are performed for three selections of initial and final states. In the first set we use zero-range initial [Eq. (9)] and zero-range final Volkov states [3] to analyze the errors introduced by the zero-range approximation. In the next set of calculations we replace the zero-range initial states with finite-range states of the atomic Hamiltonian to determine errors introduced by the use of a zero-range initial state. Finally, we consider another set of calculations again using finite-range initial states, but the plane wave components $(2\pi)^{-3/2}e^{i\mathbf{k}\cdot\mathbf{r}}$ of the final zero-range Volkov states are replaced with finite-range scattering states of the atom $\phi_{\mathbf{k}}^{(-)}(\mathbf{r})$ [23].

1. Hydrogen-like anions

In Fig. 2, we compare the predictions of the model rate to the TDSE results for the case of an s-state and exponential parameters $a = a_0/5,\ a_0/3,\ a_0$, and ∞ (a_0 is the Bohr radius) to show that the model can provide accurate results for short-range potentials at all wavelengths. For the TDSE calculations we used velocity gauge and expanded the wave function in a basis of spherical harmonics for the angular

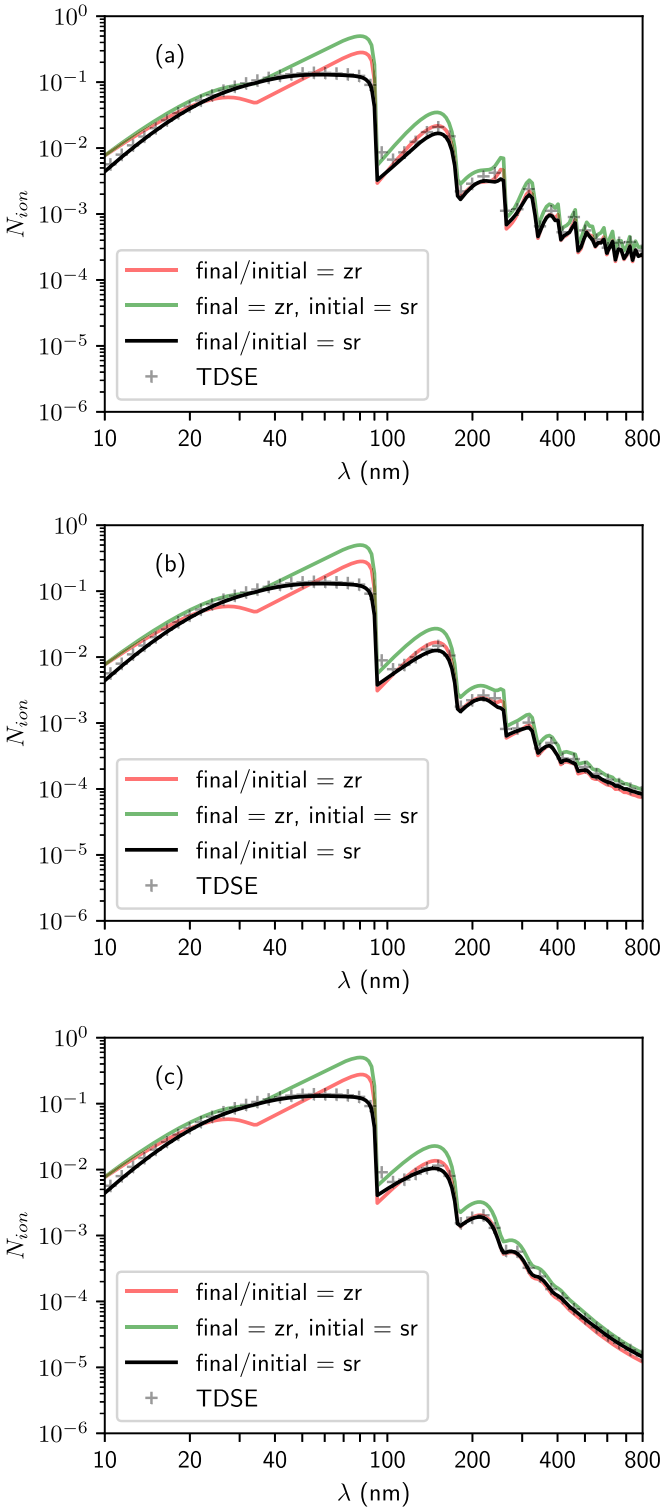

FIG. 3. Comparison of predictions for the p-state model with the TDSE results for an exponential parameter of $a = a_0/2$ for an ellipticity of (a) $\epsilon = 0$, (b) $\epsilon = 0.5$, and (c) $\epsilon = 1$. Bound-state parameters are given in Table I. Definitions of each curve and the choice of laser parameters are consistent with Fig. 2.

dimensions ($l_{\max} = |m_{\max}| = 30$) and a basis of eighth-order B splines in the radial dimension. The 600 B-spline nodes are placed such that the spacing between nodes is quadratic near the origin then becomes constant at a chosen radius (30 a.u.). The maximum radius of the box is 500 a.u., where exterior complex scaling has been applied to the last 50 a.u. of the grid. The Crank-Nicolson method has been used to propagate the wave function in time with a step size of 0.1 a.u.. Calculations have been performed for the interaction with a 16 cycle circularly polarized flat-top pulse with intensity 1×10^{14} W/cm^2 at wavelengths between 10 nm and 800 nm. An additional two cycle $\sin^2$ ramp on and ramp off has been included to the 16 cycle flat-top pulse to ensure that the vector potential smoothly goes to zero at $t \to \pm\infty$.

TABLE I. Table of bound-state energy levels and Yukawa parameters for the neon-like anion.

State	$1s$	$2s$	$2p$	$a = a_0/2$
I_p(Hartree)	33.9	1.32	0.50	$Z_c = 10.15$

For s states the predictions for the yield are essentially independent of the choice of the specific initial and final-state representation and agree well with the TDSE results for the case $a = a_0/5$ [Fig. 2(a)]. Expanding the atomic range to $a = a_0/3$ [Fig. 2(b)] and a_0 [Fig. 2(c)] makes it clear that short-range atomic initial and final (Volkov) states are required to obtain reliable results. The case of $a = \infty$ [Fig. 2(d)] is also considered, where the results based on long-range Volkov states (solid black curve) provide excellent predictions of the ionization yield for wavelengths shorter than the single-photon ionization threshold. In comparison, for any other choice of the states considered here the yield does not provide reasonable agreement at any of the wavelengths. This is exemplified by the results of the calculations using an atomic initial state and a zero-range Volkov state, which are represented by the green curve. The finite values of a were chosen such that there were no unoccupied excited states. The first-order amplitude is insufficient as excited states are introduced via an increase in range. The $a \to \infty$ limit of hydrogen should be thought of as a worst case scenario. Expansion to higher-order S-matrix elements are expected to resolve these issues [3,23,33].

2. *Neon-like anions*

For the case of a neon-like anion we chose a valence ionization potential $I_p(2\text{p}) \approx 13.6\,\text{eV}$ to enable direct comparison with the hydrogen-like data. The Yukawa range parameter of $a = a_0/2$ was chosen to obtain $1s$, $2s$, and $2p$ bound states with parameters given in Table I. To obtain the total ionization yield for the neon-like anion we assume all orbitals are occupied, neglect spin, and calculate the single orbital yield as

$$N_{\text{ion}}^{(j)} = 1 - e^{-w^{(j)}T} \tag{59}$$

as before and add those up

$$N_{\text{ion}} = N_{\text{ion}}^{(1s)} + N_{\text{ion}}^{(2s)} + N_{\text{ion}}^{(2p_1)} + N_{\text{ion}}^{(2p_0)} + N_{\text{ion}}^{(2p_{-1})} \tag{60}$$

to get the total yield. As one can anticipate, the occupied core $1s$ orbital can be neglected since the yield is much smaller than all the other yields for all wavelengths considered.

In Fig. 3 we present the results for the interaction of the neon-like anion with laser fields of different ellipticities, namely Fig. 3(a) $\epsilon = 0$ (linear polarization), Fig. 3(b) $\epsilon = 0.5$, and Fig. 3(c) $\epsilon = 1$ (circular polarization). Other laser parameters were chosen to be the same as in the calculations for the hydrogen-like anion. Comparison between the model predictions for the same choice of initial and final states and with the TDSE results, as in Fig. 2, are shown.

As in the case of hydrogen-like anion, the results show that the best agreement with the TDSE results are found using initial and final atomic states, independent of the polarization state of the laser field. Some disagreement is observed near ionization thresholds since we did not include properties of the pulse envelope in the evaluation of the model predictions. Thus, we may summarize that the exact calculation of the Keldysh ionization amplitude in length gauge can provide an excellent agreement with results of *ab initio* numerical calculations for short-range potentials. Most remarkable, this finding is independent of the angular momentum of the initial state, i.e., it holds for s as well as p states. The predictions of the present approach therefore provide a significant improvement over those of the popular saddle-point approximation, especially for initial states having an angular momentum of $l_i > 0$.

B. Photoelectron energy and angular distributions

After we have validated the accuracy of the model predictions for the total ionization yields we will now present examples for photoelectron distributions. The energy and angular distributions have been obtained using standard formulas. We evaluate the population of the ground state and each energy level in the continuum via the rate equations

$$\frac{d}{dt}\begin{bmatrix} N_i \\ N_{n_{\rm th}} \\ N_{n_{\rm th}+1} \\ \vdots \end{bmatrix} = \begin{bmatrix} -w \\ w_{n_{\rm th}} \\ w_{n_{\rm th}+1} \\ \vdots \end{bmatrix} N_i, \tag{61}$$

while the total angular distribution is given by

$$\frac{dN_{\rm ion}}{d\Omega_k} = \frac{1}{w}\frac{dw}{d\Omega_k} N_{\rm ion} = \sum_{n=n_{\rm th}}^{\infty} \frac{dN_n}{d\Omega_k} \tag{62}$$

with angular distributions for each photon process as

$$\frac{dN_n}{d\Omega_k} = \frac{1}{w_n}\frac{dw_n}{d\Omega_k} N_n, \tag{63}$$

as well as the polar distributions

$$\frac{dN_{\rm ion}}{d(\cos\theta_k)} \equiv \int_0^{2\pi} d\varphi_k \frac{dN_{\rm ion}}{d\Omega_k} = 2\pi \left.\frac{dN_{\rm ion}}{d\Omega_k}\right|_{\varphi_k=0} \tag{64}$$

and

$$\frac{dN_n}{d(\cos\theta_k)} \equiv \int_0^{2\pi} d\varphi_k \frac{dN_n}{d\Omega_k} = 2\pi \left.\frac{dN_n}{d\Omega_k}\right|_{\varphi_k=0} \tag{65}$$

for the total and the partial yields, respectively.

In Fig. 4 we plot the photoelectron energy and angular distributions for neon-like anion with both atomic initial and final states, interacting with a circularly polarized field. Wavelengths of 10 nm, 100 nm, and 800 nm have been considered. The 10 nm and 100 nm data correspond to the single-photon and perturbative multiphoton limit and, as expected, the energy distribution is linear on a log scale. In contrast, the kinetic energy distribution at 800 nm is peaked at energies larger than the threshold value $n_{\rm th}$ demonstrating the expected behavior in the nonadiabatic limit [15]. The total angular distributions correspond to emission summed over all photon processes and becomes increasingly localized around the plane of polarization as wavelengths increase due to electrons belonging to higher-order orbital angular momentum states with $l \approx m$ via the absorption of additional photons [20]. All these results qualitatively agree with the expectations for light-induced ionization in the single-photon, perturbative, and nonperturbative multiphoton regimes.

C. Short-wavelength limit

In this section we discuss and apply two ways to further approximate the model formulas, which are especially applicable in the short-wavelength regime.

1. *Restriction of orbital angular momentum states*

We first consider approximations to the coefficients in Eq. (39). Initial s states will be discussed, but similar steps may be taken for other states. The s-state coefficients are written as:

$$C_l^{\pm n}(k_n) = (i/\hbar)\frac{1}{\sqrt{2v_n}} \sum_{n_A=-\infty}^{\infty} (n_A\hbar\omega) \sum_{l_A=|m_A|}^{\infty} A_{l_A}^{m_A} K_{l_A}(k_n)\, I_0^{l_A}(k_n) \times \sum_{l_S=|m_S|}^{\infty} X_{l_S}^{m_S}(k_n) \begin{bmatrix} l & l_S & l_A \\ -(m_A+m_S) & m_S & m_A \end{bmatrix} \tag{66}$$

with $n_S = n - n_A$. The evaluation of the coefficient involves two sums over l_A and l_S, which we may interpret as a two-step absorption process. The initial state ($l_i = 0$, $m_i = 0$, for s states) is promoted to a small set of intermediate momentum states (l_A, $m_i + m_A$) via the absorption of n_A photons before an additional n_S photons are absorbed to transition into a final momentum state (l, $m_A + m_S$). We will now explore how to restrict the sums over the orbital angular momentum states.

As l_A increases the value of the integral $I_0^{l_A}(k_n) \equiv I_0^{l_A,l_A}(k_n)$ [cf., Eq. (30)] decreases due to the decreased overlap of both the continuum state $R_{k,l_A}(r)$ and the Bessel function $j_{l_A}(k_A r)$ with the initial bound state $R_i(r)$. The coefficient should therefore be dominated by the lowest-order contribution $l_A = |m_A|$. Similarly, we should expect that for the intensity and wavelengths considered the sum over l_S should be dominated by the lowest-order contribution $|m_S|$. Continuing along the same lines, the sum over l in the final rate $w_\pm$ [cf., Eq. (35)] may be restricted. This is done by choosing the set of n_A, which minimizes $|m_A| + |m_S|$ for a particular n. Geometrically this amounts to identifying the set of n_A, which minimizes the total distance ($|m_A| + |m_S|$) over which the magnetic quantum number changes from the initial state to the intermediate state ($|m_A|$) and then from the intermediate state to the final state ($|m_S|$). This is achieved for all $0 \leqslant n_A \leqslant n$ where $l = n$. Thus, the $l > n$ contributions may be neglected for fixed n since the distance $|m_A| + |m_S|$ is larger than for $n = l$ yielding the

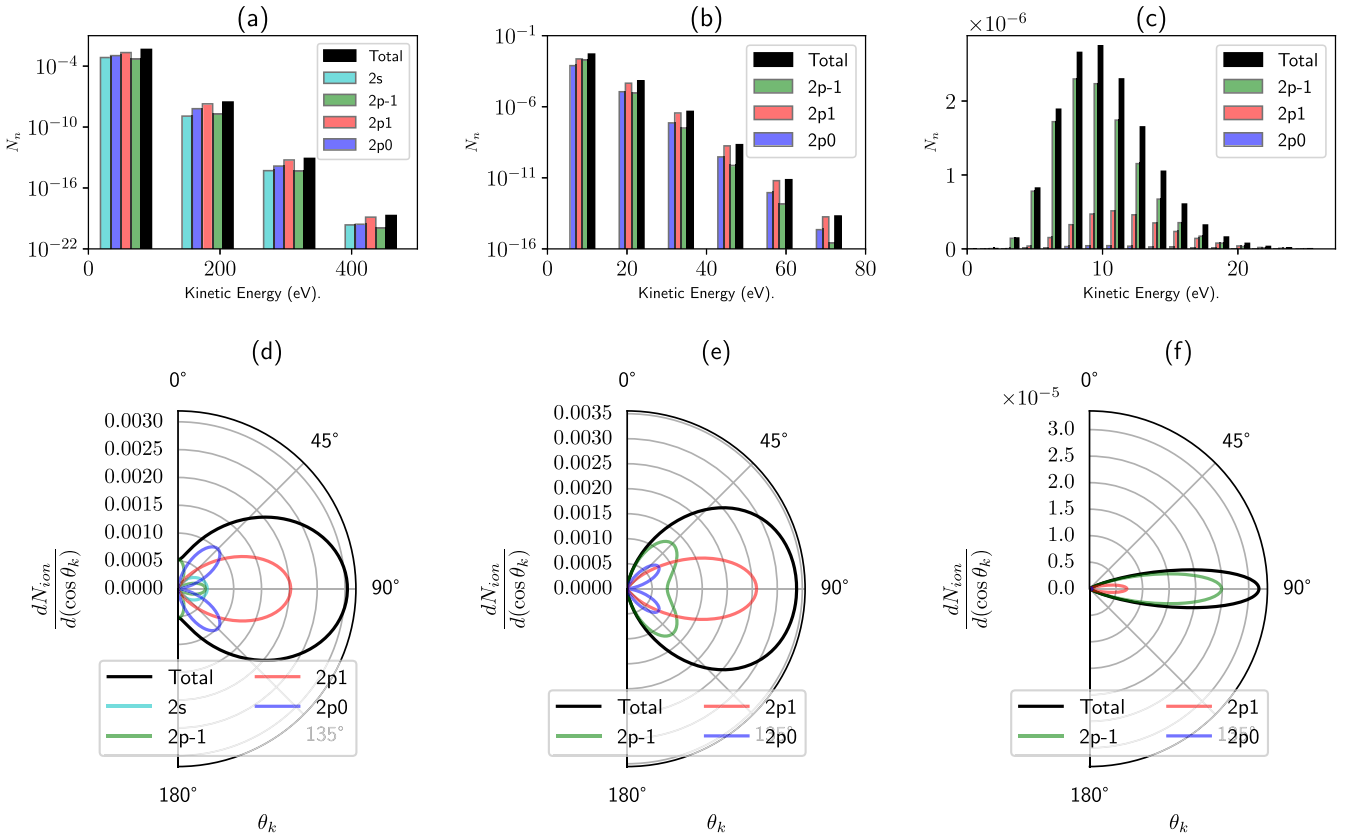

FIG. 4. (a)–(c) Photoelectron energy and (d)–(f) angular distributions for the neon-like anion data. Both finite-range initial and final (Volkov) states are chosen and wavelengths of 10 nm (a), (d), 100 nm (b), (e), and 800 nm (c), (f) are selected. Parameters are as in Fig. 3 and angular distributions correspond to the total emission summed over all photon processes.

approximation

$$w_{\pm} \approx \sum_{n=n_{\rm th}}^{\infty} w_{nn\pm}. \tag{67}$$

2. UV limit

A way to further approximate the coefficients is to consider that at the shortest wavelengths ($U_p \ll \hbar\omega$) the Bessel functions $j_{l_A}(k_A r)$ and $j_{l_S}(k_n \xi)$ are accurately approximated by their lowest-order polynomial contribution

$$j_l(x) \approx \frac{l!(2x)^l}{(2l+1)!}. \tag{68}$$

Using this additional approximation along with the restriction of the orbital angular momentum states the radial integral simplifies to

$$I_0^{|m_A|}(k_n) = \frac{C_{\kappa,0}|m_A|!}{\Gamma(l_k+3/2)}\sqrt{\frac{\kappa}{2}}\frac{(k_n k_A)^{|m_A|}}{\left(k_n^2+\kappa^2\right)^{|m_A|+1}} \tag{69}$$

with resultant coefficients

$$C_n^{\pm n}(k_n) = 2(i/\hbar)\frac{(\mp i)^n\, n!\, C_{\kappa,0}}{\sqrt{(2n+1)!}}\sqrt{\frac{\kappa}{v_n}}\frac{(k_n\xi)^n}{\left(k_n^2+\kappa^2\right)} \times (\hbar\omega)\sum_{n_A=0}^{n}\frac{n_A}{n_S!}\left(\frac{2k_A/\xi}{k_n^2+\kappa^2}\right)^{n_A}$$

$$= i\frac{C_{\kappa,0}(\mp ik_n\xi)^n}{\sqrt{(2n+1)!}}\sqrt{\frac{\hbar\kappa}{mk_n}}\left[1+\left(\frac{U_p}{n\hbar\omega}\right) \times {}_2F_0\left(-n,1;;-\frac{1}{n}\right)\right], \tag{70}$$

where the identity

$$Y_l^{\pm l}(\theta,\varphi) = \frac{1}{l!}\sqrt{\frac{(2l+1)!}{4\pi}}\left(\mp\frac{1}{2}\sin\theta e^{\pm i\varphi}\right)^l \tag{71}$$

has been applied,

$${}_2F_0(a,b;;z) = \sum_{j=0}^{\infty}\frac{(a)_j(b)_j}{j!}z^j \tag{72}$$

is a hypergeometric function, $(a)_j$ is the Pochhammer symbol, $\Gamma(a)$ is the Euler integral, and $n_S = n - n_A$ as before.

Again choosing physical parameters such that $U_p \ll \hbar\omega$ one obtains

$$C_n^{\pm n}(k_n) = i\frac{C_{\kappa,0}(\mp ik_n\xi)^n}{\sqrt{(2n+1)!}}\sqrt{\frac{\hbar\kappa}{mk_n}} \tag{73}$$

and the partial rates

$$w_{n,n\pm} = C_{\kappa,0}^2\frac{(\kappa\ v_n)\ (k_n\xi)^{2n}}{(2n+1)!}, \tag{74}$$

which gives the expected near-threshold ($l = n$) scaling of $\sim k_n^{2l+1}$ [24,31,34].

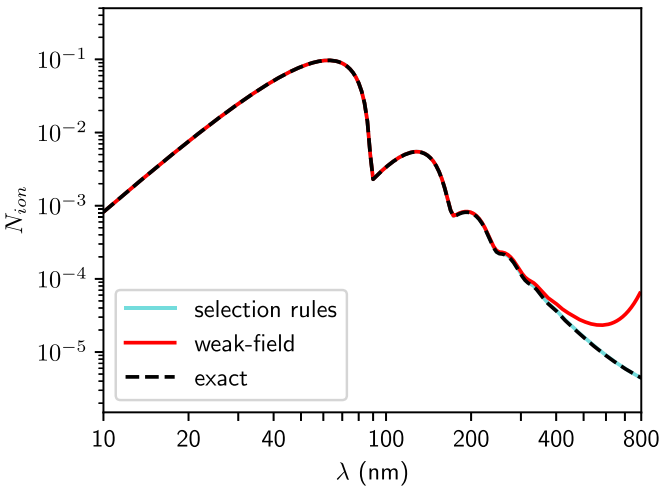

FIG. 5. Comparison between the weak-field approximation (solid red curve), exact yield (black dashed curve), and reduced set of selection rules (solid cyan curve). Laser and atomic parameters are identical to Fig. 2.

To test these two approximations we consider the zero-range ionization yield and compare the results of the approximations along with the full result in Fig. 5. Quantitative agreement is found between the exact Keldysh amplitude (black dashed lines) and the restriction of the orbital angular momentum states (solid cyan curve), as discussed in Sec. III C 1. The additional weak-field approximation (solid red curve) used in the present section provides good agreement up to the four-photon ionization process. Although applied to the present zero-range example, the restriction on orbital angular momentum states may be applied to finite-range applications as well.

IV. SUMMARY

We have presented an alternative method to evaluate the length-gauge form of the ionization amplitude in the strong-field approximation, i.e., the Keldysh amplitude. In the evaluation we circumvent the popular saddle-point approximation by expanding the amplitude in Fourier components and partial waves. Semianalytic formulas have been derived for both circular polarization and the general case of elliptical polarization. Predictions of this approach for laser-induced ionization of electrons in short-range potentials are in excellent agreement with results of simulations of the time-dependent Schrödinger equation. In particular, the predictions show a significant improvement over those obtained using the popular saddle-point approximation for initial states with angular momentum $l_i > 0$. It is further shown that this alternative approach qualitatively reproduces the trends for photoelectron energy and angular distributions.

ACKNOWLEDGMENTS

This work was primarily supported by a grant from the U.S. Department of Energy, Division of Chemical Sciences, Atomic, Molecular and Optical Sciences Program (Award No. DE-SC0001771). We also acknowledge a grant from the U.S. National Science Foundation (Grant No. PHY-1734006) for computer resources used for part of the present calculations.

APPENDIX A: EQUIVALENCE OF KELDYSH AND PPT IONIZATION AMPLITUDES

In this Appendix we will show that the first-order Kedysh amplitude is equivalent to the PPT amplitude [12] up to boundary terms for zero-range final states. To this end, we write the Keldysh amplitude as

$$\mathcal{M}^{(1)}(\mathbf{k},t) = \int_{t_0}^{t} dt_1 e^{(i/\hbar)S(\mathbf{k},t_1)}\left(-\frac{\partial}{\partial t_1}\right)\tilde{\phi}_i(\mathbf{k}(t_1)), \tag{A1}$$

where

$$\tilde{\phi}_i(\mathbf{k},\mathbf{A}(t)) = \int d\mathbf{r}_1 \overline{\phi_{\mathbf{k}+\frac{|e|}{\hbar c}\mathbf{A}(t)}(\mathbf{r}_1)}\phi_i(\mathbf{r}_1) \equiv \tilde{\phi}_i(\mathbf{k}(t)) \tag{A2}$$

and

$$\mathbf{p}(t) = \hbar\mathbf{k}(t) = \hbar\mathbf{k} + \frac{|e|}{c}\mathbf{A}(t). \tag{A3}$$

Acting on both sides with $i\hbar\frac{\partial}{\partial t}$ and using primes to denote time derivatives we see that

$$i\hbar\frac{\partial}{\partial t}[\mathcal{M}^{(0)}(\mathbf{k},t) + \mathcal{M}^{(1)}(\mathbf{k},t)] = -S'(\mathbf{k},t)\, e^{(i/\hbar)S(\mathbf{k},t)}\tilde{\phi}_i(\mathbf{k}(t)). \tag{A4}$$

Solving for the amplitude yields

$$\mathcal{M}^{(1)}(\mathbf{k},t) = -[\mathcal{M}^{(0)}(\mathbf{k},t_1)]_{t_1=t_0}^{t} + \left(\frac{i}{\hbar}\right)\int_{t_0}^{t} dt_1 S'(\mathbf{k},t_1)\, e^{(i/\hbar)S(\mathbf{k},t_1)}\tilde{\phi}_i(\mathbf{k}(t_1)), \tag{A5}$$

where the boundary term

$$\mathcal{M}^{(0)}(\mathbf{k},t) = e^{(i/\hbar)S(\mathbf{k},t)}\tilde{\phi}_i(\mathbf{k}(t)), \tag{A6}$$

can be neglected.

Using

$$S'(\mathbf{k},t) = \frac{\mathbf{p}^2(t)}{2m} + I_p \tag{A7}$$

the remaining term is written as

$$\mathcal{M}^{(1)}(\mathbf{k},t) = \left(\frac{i}{\hbar}\right)\int d^4x_1 \overline{\Phi_{\mathbf{k}}(x_1)}\left[\frac{\mathbf{p}^2(t_1)}{2m} + I_p\right]\phi_i(x_1). \tag{A8}$$

We then obtain the zero-range PPT formulas by recognizing

$$-I_p\phi_i(x) = \left[\frac{\mathbf{p}_{\rm op}{}^2}{2m} + V_a(\mathbf{r})\right]\phi_i(x), \tag{A9}$$

which gives

$$\mathcal{M}^{(1)}(\mathbf{k},t) = -\left(\frac{i}{\hbar}\right)\int d^4x_1 \overline{\Phi_{\mathbf{k}}(x_1)} \times \left[\frac{\mathbf{p}^2_{1,\rm op} - \mathbf{p}^2(t_1)}{2m} + V_a(\mathbf{r}_1)\right]\phi_i(x_1). \tag{A10}$$

Integrating by parts we see that

$$\frac{\mathbf{p}_{\rm op}^2}{2m}\Phi_{\mathbf{k}}(x_1) = \frac{\mathbf{p}^2(t)}{2m}\Phi_{\mathbf{k}}(x_1) \tag{A11}$$

gives us the desired result

$$\mathcal{M}^{(1)}(\mathbf{k},t) = -\left(\frac{i}{\hbar}\right)\int d^4x_1 \overline{\Phi_{\mathbf{k}}(x_1)} V_a(\mathbf{r}_1)\phi_i(x_1). \tag{A12}$$

For finite-range final states the situation is different. Writing down the PPT amplitude and substituting in finite-range states gives a different rate than using the equivalent Keldysh amplitude with the same states. To show this, we start with Eq. (A10) and separate the amplitude into a PPT-like contribution and a perturbation

$$\mathcal{M}^{(1)}(\mathbf{k},t) = \mathcal{M}^{(1,\rm PPT)}(\mathbf{k},t) + \delta\mathcal{M}^{(1)}(\mathbf{k},t), \tag{A13}$$

where

$$\mathcal{M}^{(1,\rm PPT)}(\mathbf{k},t) = -\left(\frac{i}{\hbar}\right)\int d^4x_1 \overline{\Phi_{\mathbf{k}}^{(-)}(x_1)} V_a(\mathbf{r}_1)\phi_i(x_1) \tag{A14}$$

and

$$\delta\mathcal{M}^{(1)}(\mathbf{k},t) = -\left(\frac{i}{\hbar}\right)\int d^4x_1 \overline{\Phi_{\mathbf{k}}^{(-)}(x_1)} \times \left[\frac{\mathbf{p}_{1,\rm op}^2 - \mathbf{p}^2(t_1)}{2m}\right]\phi_i(x_1). \tag{A15}$$

Using the Fourier representation

$$\phi_i(x) = (2\pi)^{-3/2}\int d\mathbf{k}' e^{i\mathbf{k}'\cdot\mathbf{r}}\tilde{\phi}_i(\mathbf{k}',t) \tag{A16}$$

and

$$\Phi_{\mathbf{k}}^{(-)}(x) = (2\pi)^{-3/2}\int d\mathbf{k}'' e^{i\mathbf{k}''\cdot\mathbf{r}}\tilde{\Phi}_{\mathbf{k}}^{(-)}(\mathbf{k}'',t) \tag{A17}$$

we see that the perturbation becomes

$$\delta\mathcal{M}^{(1)}(\mathbf{k},t) = -\left(\frac{i}{\hbar}\right)\int_{t_0}^{t} dt_1 \int d\mathbf{q}\, \overline{\tilde{\Phi}_{\mathbf{k}}^{(-)}(\mathbf{k}+\mathbf{q},t_1)}\left[\frac{(\hbar\mathbf{q})^2 + 2(\hbar\mathbf{k})\cdot\left(\hbar\mathbf{q} - \frac{|e|}{c}\mathbf{A}(t_1)\right) - \left(\frac{|e|}{c}\mathbf{A}(t_1)\right)^2}{2m}\right]\tilde{\phi}_i(\mathbf{k}+\mathbf{q},t_1). \tag{A18}$$

If $\phi_{\mathbf{k}}^{(-)}$ is a plane wave then the corresponding Volkov state contains a single Fourier component corresponding to $\hbar\mathbf{q} = \frac{|e|}{c}\mathbf{A}(t)$ and gives $\delta\mathcal{M}^{(1)} = 0$ as before. Atomic scattering states are described by a distribution of vectors $\mathbf{q}$, which leads to $\delta\mathcal{M}^{(1)} \neq 0$ in general and therefore a different result.

APPENDIX B: EXPANSION OF IONIZATION AMPLITUDE IN PARTIAL WAVES: CIRCULAR POLARIZATION

In this Appendix we provide the details of the evaluation of the ionization amplitude, Eq. (23). We start by expressing the vector potential contribution in $\tilde{\phi}_i(\mathbf{k},\mathbf{A}(t))$ as

$$e^{-\frac{i|e|}{\hbar c}\mathbf{A}_{\pm}(t)\cdot\mathbf{r}} = 4\pi\sum_{l_A=0}^{\infty}\sum_{n_A=-l_A}^{l_A}(-i)^{l_A} j_{l_A}(k_A r) \times \overline{Y_{l_A}^{m_A}(\hat{\mathbf{A}}_{\pm}(0))} Y_{l_A}^{m_A}(\hat{\mathbf{r}}) e^{-in_A\omega t}, \tag{B1}$$

where $k_A \equiv \frac{|e|A}{\hbar c}$ is the vector potential momentum. We note that $Y_{l_A}^{m_A}(\hat{\mathbf{r}})$ represents the angular momentum transfer with $m_A \equiv \pm n_A$ and $e^{-in_A\omega t}$ represents the total energy transfer $n_A\hbar\omega$. Since $l_A \geqslant |n_A|$, in general, n_A describes the net absorption or emission of energy and not necessarily an order of perturbation theory. Furthermore, we expand the continuum state as

$$\phi_{\mathbf{k}}^{(-)}(\mathbf{r}) = \frac{1}{k}\sum_{l_k=0}^{\infty}\sum_{m_k=-l_k}^{l_k} i^{l_k} e^{-i\eta_{l_k}(k)} R_{k,l_k}(r)\overline{Y_{l_k}^{m_k}(\hat{\mathbf{k}})} Y_{l_k}^{m_k}(\hat{\mathbf{r}}), \tag{B2}$$

where R_{k,l_k} is the radial continuum state with phase shift $\eta_{l_k}(k)$. Here $\phi_{\mathbf{k}}^{(-)}$ describes scattering states, which are asymptotically described at $r \to \infty$ by a plane wave plus an ingoing spherical wave [27].

Thus, we can evaluate

$$\left(-\frac{\partial}{\partial t}\right)\tilde{\phi}_i(\mathbf{k},\mathbf{A}(t)) = (i/\hbar)\sum_{l_A,n_A}(n_A\hbar\omega)A_{l_A}^{\pm n_A} e^{-in_A\omega t}\sum_{l_k} K_{l_k}(k) I_{l_i}^{l_k,l_A}(k) \times \begin{bmatrix} l_k & l_A & l_i \\ -(m_i+m_A) & m_A & m_i \end{bmatrix} Y_{l_k}^{m_i\pm n_A}(\hat{\mathbf{k}}) \tag{B3}$$

with coefficients

$$A_{l_A}^{m_A} \equiv 4\pi(-i)^{l_A}\overline{Y_{l_A}^{m_A}(\hat{\mathbf{A}}_{\pm}(0))}, \tag{B4}$$

and

$$K_{l_k}(k) \equiv (-i)^{l_k} e^{i\eta_{l_k}(k)}. \tag{B5}$$

The Fourier component $e^{-in_A\omega t}$ corresponds to the contributions of n_A quanta of energy to the ionized electron and the angular integrals

$$\begin{bmatrix} l_k & l_A & l_i \\ -m_k & m_A & m_i \end{bmatrix} \equiv \int d\Omega_{r_1}\overline{Y_{l_k}^{m_k}(\hat{\mathbf{r}}_1)} Y_{l_A}^{m_A}(\hat{\mathbf{r}}_1) Y_{l_i}^{m_i}(\hat{\mathbf{r}}_1) \tag{B6}$$

describe the corresponding angular momentum selection rules, which are evaluated as Wigner-3j symbols. The radial

integral

$$I_{l_i}^{l_k,l_A}(k) \equiv \frac{1}{k}\int_0^\infty dr_1\, r_1^2\, R_{k,l_k}(r_1) j_{l_A}(k_A r_1) R_i(r_1), \tag{B7}$$

determines how the initial state influences the photoelectron distribution and is numerically evaluated in the current work.

To finish the derivation we expand the action term in partial waves and perform the time integrals where

$$\begin{aligned} S_\pm(\mathbf{k},t) &= \int_0^t d\tau \left[\frac{\mathbf{p}(\tau)^2}{2m} + I_p\right] \\ &= N(k)\hbar\omega\, t + \hbar\mathbf{k}\cdot[\boldsymbol{\xi}_\pm(t) - \boldsymbol{\xi}_\pm(0)], \end{aligned} \tag{B8}$$

$$N(k) \equiv \frac{1}{\hbar\omega}(E_k + \tilde{I}_p), \quad U_p \equiv \frac{\hbar^2 k_A^2}{2m} \tag{B9}$$

and

$$\boldsymbol{\xi}_\pm(t) \equiv \frac{|e|}{mc}\int^t \mathbf{A}_\pm(\tau) d\tau = \xi[\cos(\omega t)\hat{\mathbf{x}} \pm \sin(\omega t)\hat{\mathbf{y}}] \tag{B10}$$

with $\xi \equiv \frac{|e|A}{\omega mc}$. Using the same partial-wave expansion as before we have

$$e^{i\mathbf{k}\cdot\boldsymbol{\xi}_\pm(t)} = 4\pi \sum_{l_S=0}^\infty \sum_{n_S=-l_S}^{l_S} i^{l_S} j_{l_S}(k\,\xi)\overline{Y_{l_S}^{m_S}(\hat{\boldsymbol{\xi}}_\pm(0))} Y_{l_S}^{m_S}(\hat{\mathbf{k}}) e^{-in_S\omega t} \tag{B11}$$

with $m_S \equiv \pm n_S$. For a given number of quanta n_A from the vector potential term we have

$$\begin{aligned} \int_0^t dt_1 e^{(i/\hbar)S_\pm(\mathbf{k},t_1) - in_A\omega t_1} &= e^{-i\mathbf{k}\cdot\boldsymbol{\xi}_\pm(0)} \sum_{l_S=0}^\infty \sum_{n_S=-l_S}^{l_S} X_{l_S}^{m_S}(k) Y_{l_S}^{m_S}(\hat{\mathbf{k}}) \\ &\quad \times \delta_t([N(k) - (n_A + n_S)]\omega/2) \end{aligned} \tag{B12}$$

with coefficient

$$X_{l_S}^{m_S}(k) \equiv 4\pi i^{l_S} j_{l_S}(k\xi)\overline{Y_{l_S}^{m_S}(\hat{\boldsymbol{\xi}}_\pm(0))}. \tag{B13}$$

The shape term

$$\delta_t(x) \equiv e^{ixt}\,\mathrm{sinc}(xt)\,t \tag{B14}$$

describes the distribution of final energy states after the absorption of $n_A + n_S$ photons by a finite flat-top pulse.

Combining all contribution we get for the ionization amplitude

$$\begin{aligned} \mathcal{M}_\pm^{(1)}(\mathbf{k},t) &= (i/\hbar)e^{-i\mathbf{k}\cdot\boldsymbol{\xi}_\pm(0)} \sum_{l_A=0}^\infty \sum_{n_A=-l_A}^{l_A} (n_A\hbar\omega) A_{l_A}^{m_A} \sum_{l_k=\max(|l_i-l_A|,|m_i+m_A|)}^{l_i+l_A} K_{l_k}(k)\, I_{l_i}^{l_k,l_A}(k) \begin{bmatrix} l_k & l_A & l_i \\ -(m_i+m_A) & m_A & m_i \end{bmatrix} Y_{l_k}^{m_i+m_A}(\hat{\mathbf{k}}) \\ &\quad \times \sum_{l_S=0}^\infty \sum_{n_S=-l_S}^{l_S} X_{l_S}^{m_S}(k) Y_{l_S}^{m_S}(\hat{\mathbf{k}}) \delta_t([N(k) - (n_A + n_S)]\omega/2) \end{aligned} \tag{B15}$$

with angular momentum components determined by

$$Y_{l_S}^{m_S}(\hat{\mathbf{k}}) Y_{l_k}^{m_i+m_A}(\hat{\mathbf{k}}) = \sum_l \begin{bmatrix} l & l_S & l_k \\ -(m_i+m_A+m_S) & m_S & (m_i+m_A) \end{bmatrix} Y_l^{m_i+m_A+m_S}(\hat{\mathbf{k}}) \tag{B16}$$

and yield described by

$$P_\pm^{(\mathrm{ion})}(t) = \int d\mathbf{k}\, |\mathcal{M}_\pm(\mathbf{k},t)|^2. \tag{B17}$$

It is worth noting that the amplitude may be evaluated exactly for the often-used case of zero-range Volkov states and asymptotic initial states. In that case the Bessel functions in the radial integral are expanded as

$$j_l(x) = \sqrt{\frac{\pi}{2x}} J_{l+1/2}(x) = \frac{\sqrt{\pi}}{2}\frac{(x/2)^l}{\Gamma(l+3/2)}\, {}_0F_1(;l+3/2;-x^2/4), \tag{B18}$$

with hypergeometric function

$${}_0F_1(;a;x) \equiv \sum_{m=0}^\infty \frac{x^m}{m!\,(a)_m} \tag{B19}$$

where $(a)_m \equiv \Gamma(a+m)/\Gamma(a)$ is the Pochhammer symbol and $\Gamma(a)$ is the Euler integral.

As a result, one obtains

$$\begin{aligned} I_{l_i}^{l_k,l_A}(k) &= C_{\kappa,l_i}\frac{2^{\nu-1/2}}{\kappa^{3/2}}\frac{\Gamma([l_k+l_A+\nu+2]/2)\Gamma([l_k+l_A+\nu+3]/2)}{\Gamma(l_k+3/2)\Gamma(l_A+3/2)} \\ &\quad \times \left(\frac{k}{\kappa}\right)^{l_k}\left(\frac{k_A}{\kappa}\right)^{l_A} F_4\left(\frac{l_k+l_A+\nu+2}{2}, \frac{l_k+l_A+\nu+3}{2}; l_k+\frac{3}{2}, l_A+\frac{3}{2}; -\left(\frac{k}{\kappa}\right)^2, -\left(\frac{k_A}{\kappa}\right)^2\right). \end{aligned} \tag{B20}$$

Here, the Appell F_4 function [35] is defined as

$$F_4(a,b;c_1,c_2;x,y)=\sum_{m,n=0}^{\infty}\frac{(a)_{m+n}(b)_{m+n}}{(c_1)_m(c_2)_n}\frac{x^m}{m!}\frac{y^n}{n!} \tag{B21}$$

with domain of convergence $\sqrt{|x|}+\sqrt{|y|}<1$ (or $k+k_A<\kappa$). Note that the domain can be extended via various analytic continuations [36–39].

APPENDIX C: EXPANSION OF IONIZATION AMPLITUDE IN PARTIAL WAVES: ELLIPTICAL POLARIZATION

We now provide the details of the derivation of the ionization amplitude for the general case of elliptical polarization. Again, we start with $\tilde{\phi}_i(\mathbf{k},\mathbf{A}(t))$ in Eq. (23). Following the same steps as in Appendix B we express the vector potential contribution as

$$\left(-\frac{\partial}{\partial t_1}\right)\int d\mathbf{r}_1\overline{\phi_{\mathbf{k}}^{(-)}(\mathbf{r}_1)}\,e^{-\frac{i|e|}{\hbar c}\mathbf{A}_\epsilon(t_1)\cdot\mathbf{r}_1}\phi_i(\mathbf{r}_1)=(i/\hbar)\sum_{\mathbf{l}_A,\mathbf{n}_A}(n_A\hbar\omega)A_{\mathbf{l}_A}^{\mathbf{m}_A}e^{-in_A\omega t_1}\sum_{l_k}K_{l_k}(k)Y_{l_k}^{m_k}(\hat{\mathbf{k}})I_{l_i}^{l_k,\mathbf{l}_A}(k,k_A,\epsilon)$$
$$\times\begin{bmatrix} l_k & \mathbf{l}_A & l_i\\ -(m_i+m_A) & \mathbf{m}_A & m_i\end{bmatrix}, \tag{C1}$$

where

$$A_{\mathbf{l}_A}^{\mathbf{m}_A}=16\pi^2(-i)^{l_A}\overline{Y_{l_{A_-}}^{-n_{A_-}}(\hat{\mathbf{A}}_-(0))}\,\overline{Y_{l_{A_+}}^{n_{A_+}}(\hat{\mathbf{A}}_+(0))} \tag{C2}$$

and

$$K_{l_k}(k)=(-i)^{l_k}e^{i\eta_{l_k}(k)} \tag{C3}$$

with $\mathbf{n}_A\equiv(n_{A_-},n_{A_+})$, $n_A\equiv n_{A_+}+n_{A_-}$, $\mathbf{m}_A\equiv(-n_{A_-},n_{A_+})$, $m_A\equiv n_{A_+}-n_{A_-}$, $\mathbf{l}_A\equiv(l_{A_-},l_{A_+})$, and $l_A\equiv l_{A_+}+l_{A_-}$ with similar for $A\mapsto S$. The sum $\sum_{\mathbf{l}_A,\mathbf{n}_A}$ is performed over the physical range of the four angular momentum indices l_{A_+}, n_{A_+}, l_{A_-}, and n_{A_-}.

Other contributions correspond to the angular integral

$$\begin{bmatrix} l_k & \mathbf{l}_A & l_i\\ -m_k & \mathbf{m}_A & m_i\end{bmatrix}\equiv\int d\Omega_r\overline{Y_{l_k}^{m_k}(\hat{\mathbf{r}})}Y_{l_{A_-}}^{-n_{A_-}}(\hat{\mathbf{r}})Y_{l_{A_+}}^{n_{A_+}}(\hat{\mathbf{r}})Y_{l_i}^{m_i}(\hat{\mathbf{r}}) \tag{C4}$$

expanded in terms of $3j$ symbols and the radial integral

$$I_{l_i}^{l_k,\mathbf{l}_A}(k,k_A,\epsilon)\equiv\frac{1}{k}\int_0^\infty dr_1\,r_1^2R_{k,l_k}(r_1)$$
$$\times j_{l_{A_-}}\left[\left(\frac{1-\epsilon}{2}\right)k_Ar_1\right]j_{l_{A_+}}\left[\left(\frac{1+\epsilon}{2}\right)k_Ar_1\right]$$
$$\times R_{n_i,l_i}(r_1), \tag{C5}$$

which is evaluated numerically.

The amplitude is completed by the action

$$S_\epsilon(\mathbf{k},t)=\big(E_k+I_p\big)t+\hbar\mathbf{k}\cdot[\boldsymbol{\xi}_\epsilon(t)-\boldsymbol{\xi}_\epsilon(0)]$$
$$+\frac{|e|^2}{2mc^2}\int_0^t d\tau\mathbf{A}_\epsilon(\tau)^2, \tag{C6}$$

where the ponderomotive term

$$\frac{|e|^2}{2mc^2}\int_0^t d\tau\mathbf{A}_\epsilon(\tau)^2=U_pt+\frac{|e|^2A^2(1-\epsilon^2)}{8\omega mc^2}\sin(-2\omega t) \tag{C7}$$

with

$$U_p\equiv\frac{|e|^2A^2(1+\epsilon^2)}{4mc^2} \tag{C8}$$

has now additional time-dependent oscillations due to the presence of both right- and left-handed fields.

The quiver motion

$$\boldsymbol{\xi}_\epsilon(t)=\left(\frac{1+\epsilon}{2}\right)\boldsymbol{\xi}_+(t)+\left(\frac{1-\epsilon}{2}\right)\boldsymbol{\xi}_-(t) \tag{C9}$$

is separated into left- and right-handed contributions giving the exponential partitions

$$e^{(i/\hbar)S_\epsilon(\mathbf{k},t)}=e^{-i\mathbf{k}\cdot\boldsymbol{\xi}_\epsilon(0)}e^{iN(k)\omega t}e^{i\frac{|e|^2A^2(1-\epsilon^2)}{8\hbar\omega mc^2}\sin(-2\omega t)}$$
$$\times e^{i\left(\frac{1-\epsilon}{2}\right)\mathbf{k}\cdot\boldsymbol{\xi}_-(t)}e^{i\left(\frac{1+\epsilon}{2}\right)\mathbf{k}\cdot\boldsymbol{\xi}_+(t)} \tag{C10}$$

with

$$N(k)\equiv\frac{1}{\hbar\omega}\big(E_k+\tilde{I}_p\big). \tag{C11}$$

Factors $e^{i\left(\frac{1\pm\epsilon}{2}\right)\mathbf{k}\cdot\boldsymbol{\xi}_\pm(t)}$ are evaluated as before with modified coefficients

$$X_{\mathbf{l}_S}^{\mathbf{m}_S}(k,\xi,\epsilon)\equiv16\pi^2i^{l_S}j_{l_{S_-}}\left[\left(\frac{1-\epsilon}{2}\right)k\xi\right]j_{l_{S_+}}\left[\left(\frac{1+\epsilon}{2}\right)k\xi\right]$$
$$\times\overline{Y_{l_{S_-}}^{-n_{S_-}}(\hat{\boldsymbol{\xi}}_-(0))Y_{l_{S_+}}^{n_{S_+}}(\hat{\boldsymbol{\xi}}_+(0))} \tag{C12}$$

and the new contribution

$$e^{i\frac{|e|^2A^2(1-\epsilon^2)}{8\hbar\omega mc^2}\sin(-2\omega t)}=\sum_{a=-\infty}^{\infty}B_a(A,\omega,\epsilon)e^{-2ia\omega t} \tag{C13}$$

completes the exponential with

$$B_a(A,\omega,\epsilon)=J_a\left(\frac{|e|^2A^2(1-\epsilon^2)}{8\hbar\omega mc^2}\right). \tag{C14}$$

Collecting all the terms, the finite-pulse amplitude becomes

$$\mathcal{M}_\epsilon^{(1)}(\mathbf{k},t) = (i/\hbar)e^{-i\mathbf{k}\cdot\boldsymbol{\xi}_\epsilon(0)} \sum_{\mathbf{l}_A,\mathbf{n}_A} (n_A\hbar\omega) A_{\mathbf{l}_A}^{\mathbf{m}_A} \sum_{l_k} K_{l_k}(k) I_{l_i}^{l_k,\mathbf{l}_A}(k,k_A,\epsilon) \begin{bmatrix} l_k & \mathbf{l}_A & l_i \\ -(m_i+m_A) & \mathbf{m}_A & m_i \end{bmatrix}$$
$$\times \sum_{\mathbf{l}_S,\mathbf{n}_S} X_{\mathbf{l}_S}^{\mathbf{m}_S}(k,\xi,\epsilon) \sum_l \begin{bmatrix} l & \mathbf{l}_S & l_k \\ -(m_i+m_A+m_S) & \mathbf{m}_S & (m_i+m_A) \end{bmatrix} Y_l^{m_i+m_A+m_S}(\hat{\mathbf{k}})$$
$$\times \sum_a B_a(A,\omega,\epsilon)\delta_t([N(k)-(n_A+n_S+2a)]\omega/2) \tag{C15}$$

and the yield is given by

$$P_\epsilon^{(\mathrm{ion})}(t) = \int d\mathbf{k}\, |\mathcal{M}_\epsilon(\mathbf{k},t)|^2. \tag{C16}$$

The sum $\sum_{\mathbf{l}_S,\mathbf{n}_S}$ is performed over the physical range of the four angular momentum indices l_{S_+}, n_{S_+}, l_{S_-}, and n_{S_-}.

It is again worth noting that the amplitude may be evaluated exactly for the often used case of zero-range Volkov states and asymptotic initial states. In that case the radial integral can be written as

$$I_{l_i}^{l_k,\mathbf{l}_A}(k,k_A,\epsilon) = \frac{C_{\kappa l_i}}{2^{3/2-\nu}} \frac{\sqrt{\pi}}{\kappa^{3/2}} \frac{\Gamma\left(\frac{l_k+l_A+\nu+2}{2}\right)\Gamma\left(\frac{l_k+l_A+\nu+3}{2}\right)}{\Gamma\left(l_k+\frac{3}{2}\right)\Gamma\left(l_{A_-}+\frac{3}{2}\right)\Gamma\left(l_{A_+}+\frac{3}{2}\right)} \left(\frac{k}{\kappa}\right)^{l_k} \left[\left(\frac{1-\epsilon}{2}\right)\frac{k_A}{\kappa}\right]^{l_{A_-}} \left[\left(\frac{1+\epsilon}{2}\right)\frac{k_A}{\kappa}\right]^{l_{A_+}}$$
$$\times F_C^{(3)}\left(\frac{l_k+l_A+\nu+2}{2}, \frac{l_k+l_A+\nu+3}{2}; l_k+\frac{3}{2}, l_{A_-}+\frac{3}{2}, l_{A_+}+\frac{3}{2}; -\left(\frac{k}{\kappa}\right)^2, -\left[\left(\frac{1-\epsilon}{2}\right)\frac{k_A}{\kappa}\right]^2,\right.$$
$$\left. -\left[\left(\frac{1+\epsilon}{2}\right)\frac{k_A}{\kappa}\right]^2\right), \tag{C17}$$

where

$$F_C^{(3)}(a,b;c_1,c_2,c_3;x_1,x_2,x_3) \equiv \sum_{i_1,i_2,i_3=0}^{\infty} \frac{(a)_{i_1+i_2+i_3}(b)_{i_1+i_2+i_3}}{(c_1)_{i_1}(c_2)_{i_2}(c_3)_{i_3}} \frac{x_1^{i_1}}{i_1!}\frac{x_2^{i_2}}{i_2!}\frac{x_3^{i_3}}{i_3!} \tag{C18}$$

is the Lauricella hypergeometric series [40], which may be evaluated past its radius of convergence $\sqrt{|x_1|}+\sqrt{|x_2|}+\sqrt{|x_3|}<1$ (or $k+k_A<\kappa$) through various analytic continuations.

[1] X. Guan, C. J. Noble, O. Zatsarinny, K. Bartschat, and B. I. Schneider, Comput. Phys. Commun. **180**, 2401 (2009).
[2] S.-I. Chu and D. A. Telnov, Phys. Rep. **390**, 1 (2004).
[3] L. V. Keldysh, Zh. Eksp. Teor. Fiz. **47**, 1945 (1964) [Sov. Phys. JETP **20**, 1307 (1965)].
[4] F. H. M. Faisal, J. Phys. B **6**, L89 (1973).
[5] H. R. Reiss, Phys. Rev. A **22**, 1786 (1980).
[6] M. Lewenstein, P. Balcou, M. Y. Ivanov, A. L'Huillier, and P. B. Corkum, Phys. Rev. A **49**, 2117 (1994).
[7] E. A. Seddon, J. A. Clarke, D. J. Dunning, C. Masciovecchio, C. J. Milne, F. Parmigiani, D. Rugg, J. C. H. Spence, N. R. Thompson, K. Ueda *et al.*, Rep. Prog. Phys. **80**, 115901 (2017).
[8] T. Popmintchev, M.-C. Chen, P. Arpin, M. M. Murnane, and H. C. Kapteyn, Nat. Photon. **4**, 822 (2010).
[9] O. Kfir, P. Grychtol, E. Turgut, R. Knut, D. Zusin, D. Popmintchev, T. Popmintchev, H. Nembach, J. M. Shaw, A. Fleischer *et al.*, Nat. Photon. **9**, 99 (2015).
[10] P.-C. Huang, C. Hernández-García, J.-T. Huang, P.-Y. Huang, C.-H. Lu, L. Rego, D. D. Hickstein, J. L. Ellis, A. Jaron-Becker, A. Becker *et al.*, Nat. Photon. **12**, 349 (2018).
[11] J. R. Oppenheimer, Phys. Rev. **31**, 66 (1928).
[12] A. Perelomov, V. Popov, and M. Terent'ev, Zh. Eksp. Teor. Fiz. **50**, 1393 (1966) [Sov. Phys. JETP **23**, 924 (1966)].
[13] I. Barth and O. Smirnova, Phys. Rev. A **84**, 063415 (2011).
[14] T. Herath, L. Yan, S. K. Lee, and W. Li, Phys. Rev. Lett. **109**, 043004 (2012).
[15] I. Barth and O. Smirnova, Phys. Rev. A **87**, 013433 (2013).
[16] I. Barth and M. Lein, J. Phys. B: At., Mol. Opt. Phys. **47**, 204016 (2014).
[17] A. Hartung, F. Morales, M. Kunitski, K. Henrichs, A. Laucke, M. Richter, T. Jahnke, A. Kalinin, M. Schöffler, L. P. H. Schmidt *et al.*, Nat. Photon. **10**, 526 (2016).
[18] S. Eckart, M. Kunitski, M. Richter, A. Hartung, J. Rist, F. Trinter, K. Fehre, N. Schlott, K. Henrichs, L. P. H. Schmidt *et al.*, Nat. Phys. **14**, 701 (2018).
[19] S. Walker, L. Kolanz, J. Venzke, and A. Becker, Phys. Rev. A **103**, L061101 (2021).
[20] S. Walker, L. Kolanz, J. Venzke, and A. Becker, Phys. Rev. Res. **3**, 043051 (2021).
[21] Y. Kang, E. Pisanty, M. Ciappina, M. Lewenstein, C. Figueira de Morisson Faria, and A. S. Maxwell, Eur. Phys. J. D **75**, 199 (2021).

[22] J. Dubois, C. Lévêque, J. Caillat, R. Taïeb, U. Saalmann, and J.-M. Rost, arXiv:2306.12999.
[23] F. H. M. Faisal, Phys. Rev. A **94**, 031401(R) (2016).
[24] J. M. Blatt and V. F. Weisskopf, *Theoretical Nuclear Physics* (Courier Corporation, New York, 1991).
[25] P. Brussaard and H. Tolhoek, Physica **24**, 233 (1958).
[26] M. E. Rose, *Elementary Theory of Angular Momentum* (Courier Corporation, New York, 1995).
[27] L. D. Landau and E. M. Lifshits, *Quantum Mechanics: Non-Relativistic Theory* (Pergamon Press, Oxford, 1965).
[28] K. Heyde, *Basic Ideas and Concepts in Nuclear Physics: An Introductory Approach* (CRC Press, Boca Raton, 2020).
[29] P. Lambropoulos, Phys. Rev. Lett. **29**, 453 (1972).
[30] J. Duncanson Jr., M. Strand, A. Lindgård, and R. Berry, Phys. Rev. Lett. **37**, 987 (1976).
[31] A. I. Baz', I. B. Zel'dovich, and A. Perelomov, *Scattering, Reactions and Decay in Nonrelativistic Quantum Mechanics* (Israel Program for Scientific Translations, Jerusalem, 1969).
[32] J. Bauer, Phys. Rev. A **73**, 023421 (2006).
[33] A. I. Nikishov and V. I. Ritus, Zh. Eksp. Teor. Fiz. **52**, 223 (1967) [Sov. Phys. JETP **25**, 145 (1967)].
[34] E. P. Wigner, Phys. Rev. **73**, 1002 (1948).
[35] P. Appell, Comptes Rendus **90**, 296 (1880).
[36] H. Exton, J. Phys. A: Math. Gen. **28**, 631 (1995).
[37] M. Huber, Infrared behavior of vertex functions in d-dimensional Yang-Mills theory, Diploma thesis, University of Graz, Austria, 2007.
[38] B. Ananthanarayan, S. Friot, S. Ghosh, and A. Hurier, arXiv:2005.07170.
[39] B. Ananthanarayan, S. Friot, and S. Ghosh, Phys. Rev. D **101**, 116008 (2020).
[40] G. Lauricella, Rend. Circ. Mat. Palermo **7**, 111 (1893).